Evaluating Adaptive Vertical Seismic Isolation for Equipment in Nuclear Power Plants

Mohammadreza Najafijozani[a], Tracy C. Becker[b], Dimitrios Konstantinidis[b]

[a] Department of Civil Engineering, McMaster University, Hamilton, Canada
[b] Department of Civil and Environmental Engineering, University of California, Berkeley, USA

Abstract

Seismic isolation systems are widely recognized as beneficial for protecting both acceleration- and displacement-sensitive nonstructural systems and components. So-called *adaptive* isolation systems exhibit nonlinear characteristics that enable engineers to achieve various performance goals at different hazard levels. These systems have been implemented to control the horizontal response, but there has been limited research on seismic isolation for controlling the vertical response. Thus, this paper seeks to evaluate the benefit of adaptive vertical isolation systems for components, specifically in nuclear power plants (NPP). To do this, three vertical isolation systems are designed to achieve multiple goals: a linear spring and a linear damper (LSLD), a linear spring and a nonlinear damper (LSND) and a nonlinear spring and a linear damper (NSLD). To investigate the effectiveness of the systems, a stiff piece of equipment is considered at an elevated floor within a NPP. A set of 30 triaxial ground motions is used to investigate the seismic performance of the equipment. The maximum isolation displacement and equipment acceleration are used to assess the effectiveness of the three isolation systems. While all systems significantly reduce the seismic accelerations on the equipment, the relatively simple LSLD and LSND systems exhibit superior performance over multiple hazard levels.

Keywords: earthquake, seismic risk, seismic protection, equipment isolation, equipment fragility

1. Introduction

The protection of nuclear power plants (NPP) in seismic events is crucial, and isolation can be an effective tool to help achieve acceptable performance. For example, in the 2011 Tohoku-Oki earthquake, the base-isolated emergency building in the Fukushima Daiichi plant performed well (JNSE, 2013), spurring more research on protective systems for NPP. Several studies (Huang et al., 2007, Huang et al., 2013, Kumar et al., 2015, 2017, Zhou et al., 2016) have investigated the effectiveness of base isolation in NPP. The focus of these studies has predominantly been on horizontal isolation. Despite the effectiveness of traditional isolation in reducing the horizontal seismic response of equipment, conventional seismic isolation systems are stiff in the vertical direction and thus do not reduce the vertical response. Kumar et al. (2015b) found that, while conventional base isolation can significantly decrease the horizontal demands in NPPs, the vertical response is the same as for fixed-base NPP. This has also been experimentally observed. In a shake-table-test study of a full-scale medical facility at the E-Defense facility, Furukawa et al. (2013) found that while the isolation system effectively reduced the horizontal accelerations, the vertical accelerations were amplified between the ground and the floor above the isolation layer by a factor of 1.5, and from there to the top floor by another 1.5, causing notable nonstructural

content damage. In a separate full-scale test at E-Defense, Guzman Pujols and Ryan (2018) observed that the vertical peak floor acceleration in an isolated structure with lead rubber bearings (LRB) was amplified from 2 g at the second floor to 7 g at the roof. This is compounded by large components of vertical input motions that have been underestimated for near field sites. Papazoglou and Elnashai (1996) found that in multiple earthquakes, for near-fault locations, both structural and nonstructural damage was significantly influenced by the vertical ground motion components.

To address the shortcoming of conventional isolation systems in controlling vertical accelerations, there have been attempts to provide effective 3D seismic isolation. In general, there are three approaches for 3D isolation: (1) to use 3D isolation for the whole structure at its base, (2) to use 3D isolation just for the equipment, and (3) to use horizontal isolation at the base of the structure and vertical isolation for the equipment only. In the early 2000's there was a strong push in the Japanese nuclear industry for 3D isolation at the base of the NPP. This resulted in work by Tsutsumi et al. (2000) using ball bearings for horizontal isolation and air springs for vertical, Suhara et a. (2003) using rubber bearings for horizontal isolation and air springs for vertical, and Morishita et al. (2004) using rubber bearings for horizontal isolation hydraulic devices for vertical, among others. In a non-nuclear application, 3D isolation was used in the Chisuikan residential apartment building, constructed in 2011 in Japan (Mori et al., 2012). The isolation system includes elastomeric bearings for horizontal isolation and vertical air springs and dampers for vertical isolation. However, for these 3D isolation applications, a rocking suppression device is required for this system to suppress excessive rocking motions.

Using the second approach, Nawrotzki and Siepe (2014) used helical springs, flexible in both the horizontal and vertical directions, and viscous dampers, to protect emergency diesel generators and emergency power system. They noted that the introduction of the isolation system resulted in a reduction in accelerations of up to 72%. Tsujiuchi et al. (2016) designed a vertical isolation system using horizontal springs and oblique links and cranks so as to eliminate the need for vertical springs, thus reducing the isolation system height. Lee and Constantinou (2017, 2018) developed 3D isolation systems designed for power transformers. Lee and Constantinou (2017) considered two isolation system configurations: one that allowed free rocking of the isolated equipment, and one that featured a rocking suppression system. Lee and Constantinou (2018) focused on the free-rocking configuration type because of its simplicity and effectiveness. They analytically investigated the feasibility of two free-rocking isolation systems: the first system was a horizontal–vertical integrated isolation system consisting of coil springs with an inclined linear viscous damper, and the second system consisted of a triple friction pendulum system for horizontal isolation and coil springs with a viscous damper within a telescopic guiding system for the vertical direction. The study concluded that the first system, which unlike the second system was unguided, was vulnerable to significant rocking motion, while the performance of the second system was more effective in attenuating acceleration response for both vertical and horizontal directions.

Medel-Vera and Ji (2015), who conducted a systematic review of seismic isolation for NPP, concluded that the third approach in which the entire structure is isolated horizontally at the base and only individual equipment is vertically isolated is more appealing for NPP because no rocking suppression system is required, there is no coupling between the horizontal and vertical isolation systems, and it may be more practical for maintenance. Additionally, the weight of the targeted

equipment is very low compared to the entire NPP superstructure, making the implementation of the vertical isolation practically more feasible.

For horizontal isolation systems, adaptive behavior has been proposed to meet multiple objectives under increasing levels of ground motion excitation (Fenz and Constantinou, 2007 , Morgan and Mahin 2010, Yang et al., 2010, Becker et al., 2017, Van Engelen et al., 2016). The adaptability of these systems is derived from the physical configuration or material properties of the systems. However, research in adaptive vertical isolation systems is still new. Cimellaro et al. (2019), Meng et al. (2015) and Zhou et al. (2019) studied the application of negative or quasi-zero stiffness devices proposed for vertical vibration mitigation for light, sensitive equipment. In an opposite approach, Ueda et al. (2007) and Wakabayashi et al. (2009) proposed vertical softening isolation systems through the use of Λ and V-shaped links, respectively, in an effort to reduce static displacement while maintaining flexibility under larger earthquakes. Asai et al. (2008) used constant load springs under the equipment which also results in a softening system where the transmitted load and therefore the equipment acceleration is limited through the spring load design.

The ability and efficiency of these vertical adaptive systems to achieve multiple goals has not been comprehensively compared. Given the wide variety of approaches for vertical isolation, it is difficult know which behavior will provide greatest benefit for the equipment. Thus, this paper investigates if indeed, and to what degree, adaptive vertical isolation systems are useful for acceleration sensitive equipment in NPP. To this end, three systems are studied: a linear spring and a linear damper (LSLD), a linear spring and nonlinear damper (LSND), and a nonlinear spring with a linear damper (NSLD). Design methodologies for the vertical isolation systems are presented with the performance goals of the equipment in mind, and the performance of three systems are compared.

2. Nuclear power plant structure and component of interest

The effectiveness of the various vertical isolation systems on the seismic performance of a piece of equipment is evaluated in a representative NPP structure that is isolated horizontally at the base. This section discusses the superstructure and horizontal base isolation model of the NPP, as well as the design spectra, and the suite of ground motions used in the response history analysis of the NPP. The vertical isolation systems considered are presented in subsequent sections.

2.1. Nuclear power plant internal structure model

The internal structure of the NPP is represented by a simplified 3D lumped-mass stick model (Saudy, 2017), which is adapted in OpenSees (OpenSees, 2018) for the purposes of this study, as shown in Fig. 1. The node coordinates, masses, and element stiffnesses are presented in Appendix A of Najafijozani (2019). The lumped mass nodes are connected to the internal structure by rigid elements. The total mass of internal structure is 50,000 ton. The height of internal structure is 39 m. The natural frequencies of the first and second modes of the fixed-base model are 7.14 Hz (0.14 s) and 7.69 Hz (0.13 s), respectively. The frequency of the twelfth mode of the superstructure, which corresponds to the first vertical mode, is 21.14 Hz (0.0473 s). Rayleigh damping is used with 5% damping for the first and twelfth modes. Further information about the internal structure can be found in Huang et al., 2008, which used the same internal structure model.
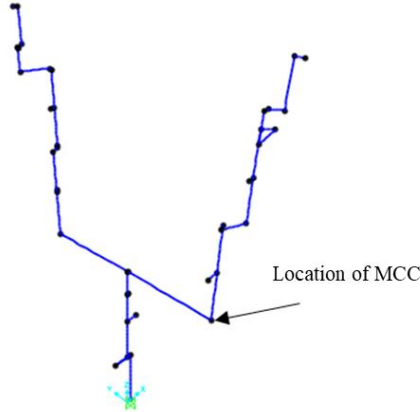
Fig. 1. Lumped mass stick model of the internal structure of a NPP and the location of the motor control center (MCC)

2.2. Design spectra

The NPP is assumed to be located at the Diablo Canyon NPP site in California. The process outlined in ASCE 43-05 (2005) was used to determine the horizontal design response spectra for the design basis earthquake (DBE) with a return period of 10,000 years. The design response spectrum is found by multiplying the uniform hazard response spectra by the design factor. The design factor is the maximum of DF_1 and DF_2 (ASCE 43-05, 2005). Table 2-1 in ASCE 43-05 (2005) specifies the value of $DF_1 = 1$ for seismic design category 5, to which NPP are assigned. The second design factor is

$$DF_2 = 0.6 \, (A_R)^{\beta} \tag{1}$$

where β is 0.8 for seismic design category 5 (ASCE 43-05, 2005), and A_R is a slope factor found at each frequency of the uniform hazard spectra found as

$$A_R = \frac{SA_{0.1H_D}}{SA_{H_D}} \tag{2}$$

where SA_{H_D} is the spectral acceleration at the mean annual frequency of exceedance, $H_D = 1 \times 10^{-4}$, $SA_{0.1H_D}$ is the spectral acceleration at $0.1H_D$. DF2 is less than one across all frequencies; thus, as $DF_1 = 1.0$, the design factor is taken as 1.0. The vertical to horizontal pseudo acceleration ratio for near field motions recommended by ASCE 43-05 (2005) is used to determine the vertical design response spectra. This ratio is 2/3 at frequencies below 3 Hz, one for frequencies above 5 Hz, and transitions from 2/3 to 1 for frequencies between 3 Hz and 5 Hz. Fig. 2 shows the horizontal and vertical DBE spectra.
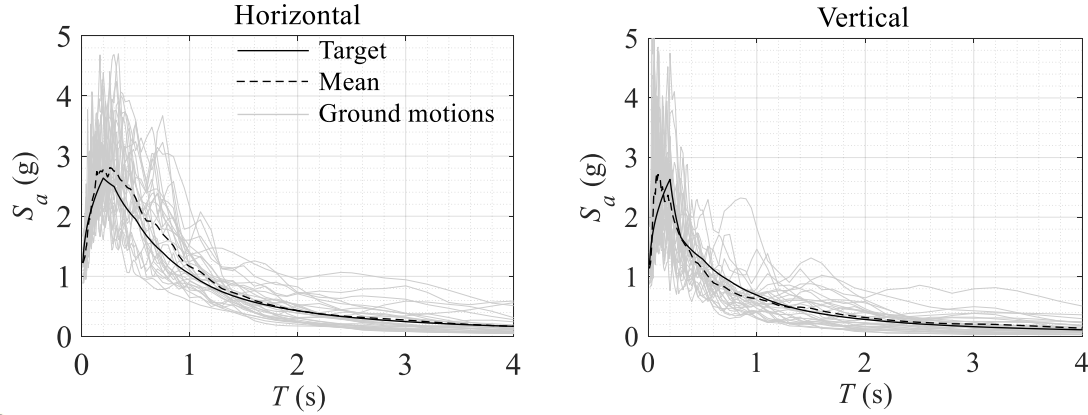
Fig. 2. Horizontal (left) and vertical (right) target and mean response spectra at DBE level and 5% damping

2.3. Horizontal base isolation of the NPP

A horizontal isolation system with effective period and damping ratio of 2.5 s and 20% at the DBE level is designed for the horizontal isolation at the base of the NPP. The system consists of 150 lead rubber bearings (LRB), the properties of which are summarized in Table 1; the force-displacement relationship of the bearings is shown in Fig. 3.

Table 1: Design parameters of the LRB

| Demands	Value
d (displacement demand)	0.5 m
d_y (yielding displacement)	0.027 m
Material properties	
G (shear modulus)	0.4 MPa
K (bulk modulus)	2,000 MPa
σ_L (yield strength of lead)	8.5 MPa
Geometric properties	
D (bearing diameter)	1.178 m
D_L (diameter of the lead core)	0.22 m
S (shape factor)	20
H (height of the LRB)	0.56 m
t_r (total thickness of rubber)	0.34 m
Physical properties	
Q_d (characteristic strength)	343 kN
K_1 (initial stiffness)	14,040 kN/m
K_2 (post-yield stiffness)	1,404 kN/m
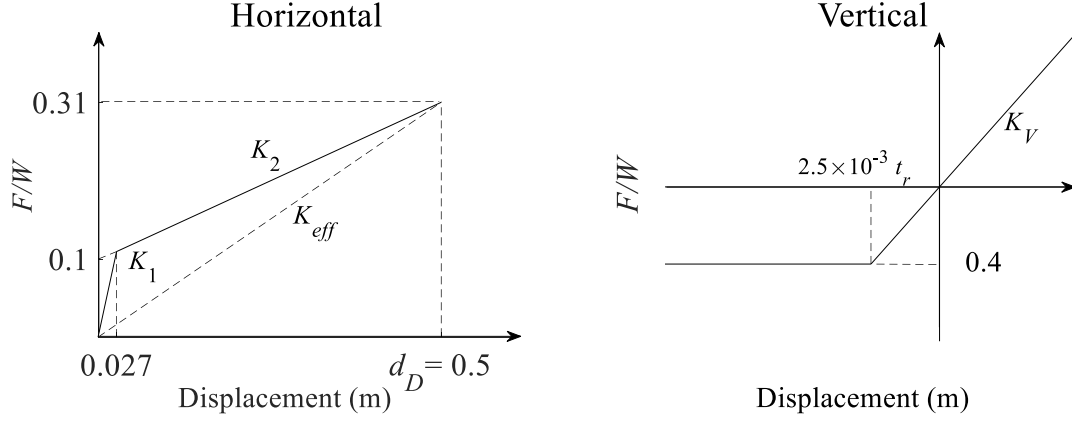
Fig. 3. Force-displacement relation of the LRB in the horizontal and vertical directions (positive displacement indicates compression)

The post-yield stiffness of the LRB in the horizontal direction is (McVitty and Constantinou, 2015)

$$K_2 = f_L \frac{GA}{t_r} \tag{3}$$

where G is the shear modulus of the elastomer, A is the area of the bearing, t_r is the total thickness of the rubber, and f_L is an experimental parameter for the effect of lead on the post-yield stiffness, taken as between 1.0 to 1.2 (McVitty and Constantinou, 2015). Here, this parameter is assumed to be 1.1.

The vertical stiffness of the LRB in compression is determined from

$$K_V = \frac{E_c A}{t_r} \tag{4}$$

where E_c is the compression modulus, which for an annular pad is given by (Constantinou et al., 1992; Kelly and Konstantinidis, 2011)

$$E_c = K \left[1 + C_1 \left(I_1(\vartheta) - \eta I_1(\eta \vartheta) \right) + C_2 \left(K_1(\vartheta) - \eta K_1(\eta \vartheta) \right) \right] \tag{5}$$

where K is the bulk modulus, $\eta = D_L / D$, and

$$\vartheta = \sqrt{\frac{48G}{K}} \frac{S}{1 - \eta} \tag{6}$$

$$C_1 = \frac{1}{\sqrt{\frac{12\,G}{K}}(1+\eta)\,S} \frac{K_0(\vartheta) - K_0(\eta \vartheta)}{I_0(\vartheta)\,K_0(\eta \vartheta) - I_0(\eta \vartheta)\,K_0(\vartheta)} \tag{7}$$

$$C_2 = \frac{1}{\sqrt{\frac{12\,G}{K}}(1+\eta)\,S} \frac{I_0(\vartheta) - I_0(\eta \vartheta)}{I_0(\vartheta)\,K_0(\eta \vartheta) - I_0(\eta \vartheta)\,K_0(\vartheta)} \tag{8}$$

where, S is the shape factor, I_0 and I_1 are modified Bessel functions of the first kind and order 0 and 1, and K_0 and K_1 are modified Bessel functions of the second kind and order 0 and 1. With $G = 0.4$ MPa, $S = 20$, and $\eta = 0.2$, the compression modulus, is $E_c = 2.9GS^2$.

Rearranging Equations (3) and (4) leads to

$$K_V = \frac{2.9\,S^2}{f_L}\,K_2 \tag{9}$$

for the particular LRB design. Substituting in $S = 20$ and $f_L = 1.1$ gives $K_V/K_2 = 1{,}160$.

A bilinear elastic model is used to capture the reduction in stiffness that occurs when the rubber experiences cavitation in tension. Gent (1990) proposed that the onset of cavitation occurs at negative pressure of $3G$. Hence, the cavitation strain is $3G/E_c = 3G/2.9GS^2 = 2.5\times10^{-3}$ (Fig. 3). The post-cavitation stiffness in this study is assumed to be zero. Damping in the LRB isolators in the vertical direction is neglected.

The OpenSees model of the superstructure shown in Fig. 1 is modified to include the LRB isolators at its base. The horizontal behavior shown in Fig. 3 (left) is modeled using the *elastomericBearingPlasticity* element, while the vertical behavior in Fig. 3 (right) is modeled using the *ElasticMultiLinear* element. Although advanced numerical models for LRBs are available in OpenSees (e.g., *LeadRubberX* (Kumar et al., 2015)), they are not used in the current study where the focus is placed on a comparison of different *vertical* equipment isolation system, while keeping the horizontal modeling of the LRB isolation system at the base of the NPP simple. Modal analysis shows that the first six fundamental frequencies of the isolated NPP are 0.398 Hz (horizontal), 0.399 Hz (horizontal), 8.62 Hz (rotational), 8.66 Hz (torsional), 9.16 Hz (rotational) and 10.42 Hz (vertical). Without considering the effect of vertical stiffness of the LRB system, the first mode in the vertical direction is the twelfth mode at 21.16 Hz. Consequently, the effect of vertical stiffness of the dynamics of the LRB-isolated NPP is not negligible and therefore is accounted for in the analysis.

2.4. Ground motion selection and scaling

To evaluate the performance of the different equipment vertical isolation systems, thirty ground motions are selected and scaled from PEER NGA West 2. The ground motion characteristics were based on a deaggregation of the Diablo Canyon, CA site. All motions have a magnitude in the range from 6 to 8 and rupture distance from 0 to 20 km. The values for V_{s30} of the selected motions were consistent with an assumed site class C. The specific ground motions and their scaling can be found in Najafijozani (2019). As ASCE 4-16 (2016) does not specify the period range over which to scale the ground motions, the range form ASCE 7-16 (2016) is used but expanded to cover both superstructure as well as isolation frequencies: $0.2T_f$ to $1.5T_b$, where T_f and T_b are the fundamental periods of the NPP superstructure and the base-isolated NPP. The fundamental periods of the NPP superstructure are 0.14 s and 0.0473 s in the horizontal and vertical directions, respectively. The fundamental periods of the base isolated NPP are 2.5 s and 0.09 s in the horizontal and vertical directions, respectively. Hence, the scaling ranges are from 0.03 to 3.75 s for the horizontal ground motions and from 0.001 to 0.15 s for the vertical ground motions. Fig. 2

shows the individual and mean response spectra of the ground motions in the horizontal and vertical directions.

2.5. Equipment of interest

A motor control center (MCC), which is described as a "very important electrical equipment with low seismic capacity" (Bandyopadhyay and Hofmayer, 1986), is selected as the targeted component to be isolated vertically. MCCs control numerous safety-related equipment in NPP. It is assumed that the MCC is attached at the location shown in Fig. 1. The fundamental frequencies of the MCC in the two horizontal directions and the vertical direction are 5.8, 4.8, and 20 Hz, respectively (Radford, 2015). The vertical isolation system is introduced between the floor and the MCC.

3. Performance objectives

ASCE 4-16 (2016) specifies performance expectations (objectives) for isolated nuclear structures. While objectives are given for DBE and beyond design basis earthquake (BDBE), defined as 150% of DBE level, the objectives address only the horizontal isolation. The commentary of ASCE 4-16 (2016) specifically notes this and cites the lack of standard commercially available vertical isolation systems. Due to the lack of clearly defined and accepted performance criteria for vertical isolation systems, the ASCE 4-16 (2016) objectives for horizontal isolation are used in this research for the vertical isolation system. Table 2 lists the performance objectives of the isolation system and other structures, systems, and components (SSCs). These performance objectives will be used to determine the target peak vertical accelerations under the DBE and BDBE levels and the isolation system displacement under the BDBE earthquake to be used in the design of the systems.

Table 2: Performance expectations for seismically isolated structures

Item	DBE	BDBE
Isolation system	No damage to the isolation system.	Greater than 90% probability of the isolation system surviving without loss of gravity-load capacity.
Other SSCs	Greater than 99% probability that component capacities will not be exceeded.	Greater than 90% probability that component capacities will not be exceeded.

3.1. Equipment

Bandyopadhyay and Hofmayer (1986) carried out experimental tests on the MCC and found three failure modes: contact chatter voltage drop-out, change of state of starter auxiliary contact, and change of state of starter main contact. In this section, the corresponding acceleration fragility functions are computed, from which the accelerations corresponding to 1% and 10% probability of these failures occurring can be determined. The capacity of a component is expressed as (Reed and Kennedy, 1994)

$$A = \overline{A}\, \varepsilon_r = \widehat{a}\, \varepsilon_u \varepsilon_r \qquad (10)$$

where A is the random variable of the capacity of the component, $\overline{A}$ is the random variable of the median capacity of the component, $\widehat{a}$ is the median of $\overline{A}$, ε_r and ε_u are lognormally distributed random variables with medians equal to one and standard deviations of β_r and β_u, which are representative the aleatoric randomness and epistemic uncertainty, respectively. The probability density function of $\overline{A}$ is

$$Q = \Phi\left(\frac{\ln \widehat{a} - \ln \overline{a}}{\beta_u}\right) \qquad (11)$$

where Q is the probability (confidence level) that $\widehat{a}$ exceeds the given value $\overline{a}$, and Φ is the standard normal distribution function. Rearranging Equation (11) leads to

$$\overline{a} = \widehat{a}\, e^{-\Phi^{-1}(Q)\beta_u} \qquad (12)$$

The fragility curve is defined as

$$f = \Phi\left(\frac{\ln a - \ln \overline{a}}{\beta_r}\right) \qquad (13)$$

where f is the probability of failure of the component, and a is the demand. Combining Equation (12) and (13) gives

$$f = \Phi\left(\frac{\ln \dfrac{a}{\widehat{a}} + \Phi^{-1}(Q)\beta_u}{\beta_r}\right) \qquad (14)$$

The confidence level parameter (Q) is assumed 0.5 here (Huang et al., 2011). The recommended median horizontal acceleration and associated dispersion for the fragility functions for the failure modes in Bandyopadhyay and Hofmayer (1986) are presented in Table 3. Equation (14) is used to draw the fragility curve corresponding to each failure mode. Fig. 4 shows the fragility curves of the three failure modes of the MCC, where *peak equipment acceleration* is defined here to be the peak absolute acceleration at the base of equipment. Although these fragility curves are based on horizontal acceleration values and test protocol input motion that is different from the motion

Table 3:   Fragility parameters of failure modes of the MCC

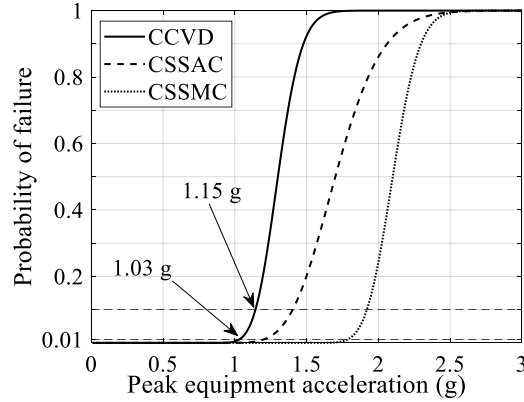| Failure Mode	$\widehat{a}$	β_u	β_r
Contact chatter voltage drop-out (CCVD)	1.3	0.20	0.10
Change of state of starter auxiliary contact (CSSAC)	1.7	0.17	0.15
Change of state of starter main contact (CSSMC)	2.1	0.33	0.07

Fig. 4. Fragility curves for the MCC failure modes: contact chatter voltage drop-out (CCVD), change of state of starter auxiliary contact (CSSAC), and change of state of starter main contact (CSSMC)

the MCC would experience atop the vertical isolation system in this study, they are used herein in the absence of more appropriate fragility information, simply to obtain a reasonable reference design. The acceleration limits under the two hazard levels are 1.03 g and 1.15 g, respectively, as shown in Fig. 4. Both limits are based on contact chatter voltage drop-out.

3.2. Vertical seismic isolation system

To ensure that the isolation system has a 90% probability of surviving the BDBE, the maximum allowable displacement must be found. In the vertical direction, there are three possible failure modes: yielding, pounding, and buckling. The minimum displacement that causes one of these failure modes is taken as the maximum allowed displacement. As the dispersion of the code response spectrum is unknown, ASCE 4-16 (2016) allows the spectrum of the 90th percentile of the BDBE to be calculated by multiplying the DBE spectrum by 3.

4. Vertical seismic isolation systems

The MCC is isolated vertically between the floor and the equipment. Hybrid 3D isolation systems for equipment like the one proposed by Lee and Constantinou (2018) aim to reduce both large horizontal and large vertical accelerations. In the approach taken in the current study, however, at the location of the vertical isolation system, the horizontal component of the floor excitation is low because the NPP is horizontally isolated at its base through the use of the LRB system. Specifically, the LRB system manages to achieve a reduction from 1.22 g horizontal peak ground acceleration to 0.32 g horizontal peak floor acceleration at the DBE level. Because of this, it is assumed that the rocking response is negligible. In practice this should be checked, and if shown to be an issue, a rocking suppression system that guides the isolation platform to only move vertically, such as that used by Lee and Constantinou (2017), may be implemented. Therefore, this section focuses on controlling the seismic response of the equipment in the vertical direction only. Three vertical isolation systems are designed to achieve the performance goals outlined in Section 3. The three systems consist of in-parallel configurations of linear and nonlinear springs and dampers as follows: (a) linear spring and linear damper (LSLD); (b) linear spring and nonlinear damper (LSND), and (c) nonlinear spring and a linear damper (NSLD). All springs, whether linear or nonlinear, are elastic, and no hysteretic damping is used. Furthermore, the design of the system

should include a vertical guiding system. Although the design of the vertical guiding system is not explicitly considered in this study, a simple such system could potentially consist of stainless- steel shafts extending up from the floor and wrapped by PTFE-lined collars attached to the isolation platform. For comparing the performances, all these systems are designed such that they are equivalent under the BDBE level. Fig. 5 and 6 show the ground response spectra and the floor response spectra for acceleration and displacement response spectra at the location of the MCC (Fig. 1) under DBE and BDBE levels, which are used to aid in the design of the vertical isolation systems.
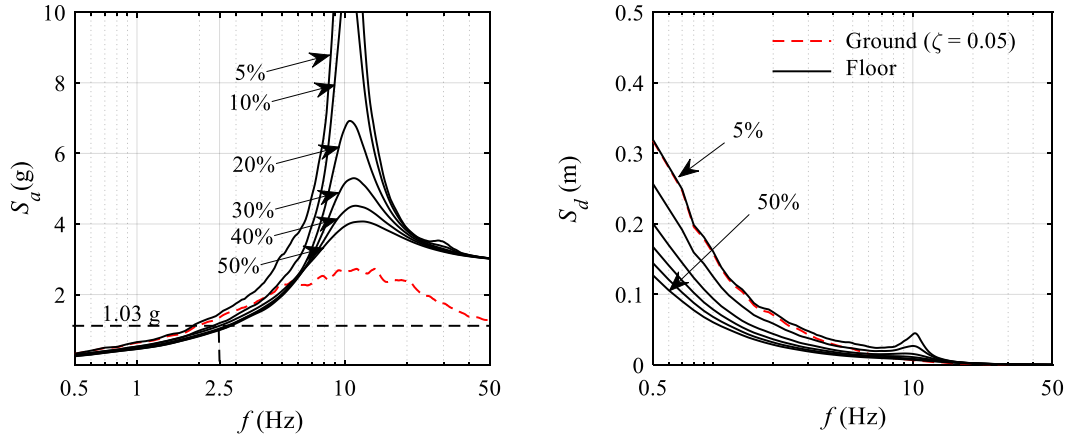
Fig. 5. DBE level mean vertical ground and floor response spectra of the ground motions at the location of the equipment.
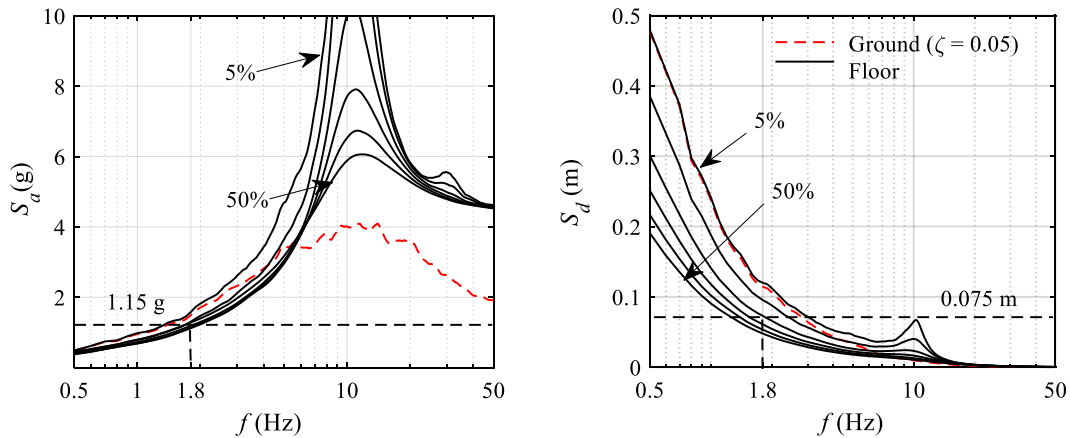

Fig. 6. BDBE level mean vertical ground and floor response spectra of the ground motions at the location of the equipment.

The peak ground acceleration in the vertical direction is 1.1 g at the DBE level, which is amplified to 3.0 g at the location of MCC. This large amplification is expected, especially as the vertical fundamental frequency of the base isolated NPP (10.42 Hz) is close to the peak of the vertical ground motions. This amplification is rather insensitive to the design of the LRB in the vertical direction, as the vertical ground response spectrum (dashed line in Fig. 5 (left)) has fairly constant spectral accelerations throughout the range of 5 to 20 Hz, which covers the frequencies of possible

LRB designs with shape factor values ranging from roughly 10 to above 50. This clearly highlights the need for vertical isolation of the equipment at the floor level.

4.1 Linear spring and linear damper

The damping of the LSLD isolation system is chosen to be $\xi_s = 20\%$ because more damping does not further decrease accelerations (see Fig. 5 (left)) and has minor impact on displacement (Fig. 5 (right)). From Fig. 5 (left), to meet the target of 1.03 g spectral acceleration under the DBE level, the vertical isolation system must have a frequency of less than 2.5 Hz. However, to achieve 1.15 g under the BDBE level (see Fig. 6 (left)), the frequency must be less than $f_s = 1.8$ Hz. At this frequency an equipment acceleration of 0.75 g under the DBE level is achieved. Hence, this frequency value is selected for the LSLD system, and the damping coefficient required to achieve $\xi_s = 20\%$ viscous damping ratio is then $c_1 = 4\pi m f_s \xi_s = 1{,}627$ Ns/m.

The total stiffness of the vertical isolation system is

$$K_t = 4\pi^2 m f_s^2 \tag{15}$$

where $m = 360$ kg is the mass of the MCC. The isolation system is designed with four springs ($N = 4$), and the individual stiffness of each helical spring is (Shigley, 2011)

$$K_i = \frac{K_t}{N} = \frac{G_s d_w^4}{8 D_s^3 n_a} \tag{16}$$

where G_s is the shear modulus of steel (79 GPa), d_w is the diameter of the wire, D_s is the diameter of the spring, $n_a = n - 2$ is the number of active coils, and n is the total number of coils.

The mean resulting dynamic displacement demands of the isolation system are 0.05 and 0.073 m under DBE and BDBE levels, respectively (Fig. 5 and 6). The total displacement demand is the summation of the static displacement under gravity and the dynamic displacement. The static displacement can be expressed by

$$u_{\text{st}} = \frac{g}{4\pi^2 f_s^2} \tag{17}$$

which is 0.076 m for the selected frequency. Consequently, the mean total displacement demands are 0.126 and 0.149 m under the DBE and BDBE levels. Using the recommendation of ASCE 4-16 (2016), the dynamic displacement demand corresponding to the 90% percentile of the BDBE is taken as three times the displacement under the DBE (0.05 m) (Table 2). Thus, the compressive displacement demand for the vertical isolation system is $u_d = 3 \times 0.05 + 0.076 = 0.226$ m. In tension, the displacement demand is $3 \times 0.05 = 0.15$ m. The displacement capacity of helical springs can be found as (Becker and Cleghorn, 1992, Shigley, 2011)

$$u_{max} = \min\left\{ u_y = \frac{\tau \pi D_s^2 n_a}{G_s d_w}, \ u_b = 0.812\, l \left(1 - \sqrt{1 - 6.87\left(\frac{2D_s}{l}\right)^2} \right), \ u_l = l - n\, d \right\} \tag{18}$$

where u_y, u_b, and u_l are the yield displacement, buckling displacement, and free length minus solid length of the spring, τ is the permissible shear stress (550 MPa), and l is the free length of the spring. Equation (18) shows that buckling will not occur when the ratio l / D_s is less than 5.24. Table 4 shows the design specifications of the linear spring. The l / D_s for this design is 4.03, and thus, buckling will not occur.

Table 4: Design parameter of each helical spring

Material properties	Value
G_s (shear modulus of steel)	79 GPa
Geometric properties	
D_s (mean diameter of spring)	100 mm
d_w (diameter of wire)	11 mm
l (free length)	406 mm
n (number of coils)	14
Capacity	
u_y (yield displacement)	240 mm
u_l (= $l - nd$)	251 mm
u_{max} (displacement capacity)	240 mm
Demand	
u_d (displacement demand)	226 mm

4.2 Linear spring and nonlinear damper

The spring of the LSLD system with frequency 1.8 Hz is used in the LSND system. The seismic design of the nonlinear damper in the LSND system is based on two parameters: the damping ratio ξ_N at each hazard level and the nonlinear exponent parameter α. The typical range of this parameter for seismic isolation is in the range 0.35-1.0 (Asher et al., 1996, Lin and Chopra, 2002). Nonlinear dampers with α in the range of 1.0-2.0 are usually used as shock-absorbers (Christopoulos and Filiatrault, 2008). The values of 0.5 and 1.5 are selected for the parameter α in this research. The force in the nonlinear viscous damper, F_D, is expressed by

$$F_D = c_\alpha \, |\dot{u}|^\alpha \text{sign} \, (\dot{u}) \tag{19}$$

where c_α is the damping coefficient of the nonlinear damper, and $\dot{u}$ is the velocity.

To establish equivalency between the linear and nonlinear viscous damper, their energies dissipated per cycle (E_L and E_N respectively) of harmonic motion with displacement amplitude $u_0 = 0.073$ m (i.e., the BDBE displacement), and forcing frequency $\omega = 2\pi f_s = 11.304$ s^{-1} (i.e., the natural frequency of the system), are set equal to each other. Using (Soong and Constantinou, 1994):

13

$$E_L = c_1 \pi \omega u_0^2 \tag{20}$$

$$E_N = 2\sqrt{\pi} c_\alpha u_0^{\alpha+1} \omega^\alpha \frac{\Gamma\left(1+\frac{\alpha}{2}\right)}{\Gamma\left(\frac{3}{2}+\frac{\alpha}{2}\right)} \tag{21}$$

where Γ is the gamma function, the following ratio is obtained:

$$\frac{c_\alpha}{c_1} = \frac{\sqrt{\pi}}{2} (u_0 \omega)^{1-\alpha} \frac{\Gamma\left(\frac{3}{2}+\frac{\alpha}{2}\right)}{\Gamma\left(1+\frac{\alpha}{2}\right)} \tag{22}$$

and, using $c_1 = 2m\omega\xi_s$,

$$c_\alpha = \xi_s \sqrt{\pi} m \omega^{2-\alpha} u_0^{1-\alpha} \frac{\Gamma\left(\frac{3}{2}+\frac{\alpha}{2}\right)}{\Gamma\left(\frac{1}{2}+\frac{\alpha}{2}\right)} \tag{23}$$

Since $\xi_s = 0.2$ and $m = 360$ kg, the damping coefficient of the LSND system with $\alpha = 0.5$ and 1.5 is $c_\alpha = 1{,}328$ N(s/m)$^{0.5}$ and $1{,}957$ N(s/m)$^{1.5}$, respectively. The equivalent damping ratio at the DBE level can be obtained by rearranging Equation (23) and using $u_0 = 0.05$ m. The damping ratio at the DBE level is 0.25 and 0.16 for $\alpha = 0.5$ and $\alpha = 1.5$ (Table 5).

4.3 Nonlinear spring and linear damper

Nonlinear springs allow the designer to target different effective natural frequencies under increasing hazard levels to achieve multiple performance goals. Fig. 7 shows potential nonlinear springs and their related force-displacement relations. In this figure, d is total displacement (summation of static and dynamic displacement). Ueda et al. (2007) proposed a vertical isolation system consisting of Λ-shaped link with softening behavior in compression. In contrast to V-shaped link springs, conical springs show hardening behavior in compression (Rodriguez et al., 2006, Wu and Hsu, 1998). A cone disk under compressive displacement exhibits softening behavior that goes into a negative stiffness region, followed by hardening behavior. By choosing proper values, the combination of linear spring and cone disk can generate symmetrical hardening behavior centered around the static equilibrium point, as proposed by Meng et al. (2015) and Zhou et al. (2019).The combination of a conical spring and Λ-link with a gap can achieve symmetrical softening behavior at the static equilibrium.

To design the nonlinear spring systems, a bilinear elastic spring is considered with initial stiffness K_1 and second stiffness K_2. Because the system is nonlinear, effective parameters are used in its design; namely K_D, f_D, and ξ_D, are the DBE level effective stiffness, effective frequency, and effective damping ratio, while K_B, f_B, and ξ_B, are the corresponding parameters at the BDBE level. In this study, it is chosen that the displacement at which the transition between K_1 and K_2 occurs is the DBE level displacement u_D. Therefore, the effective stiffness of the
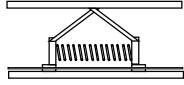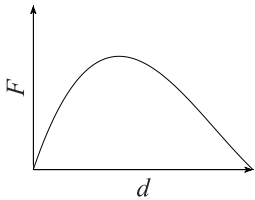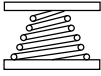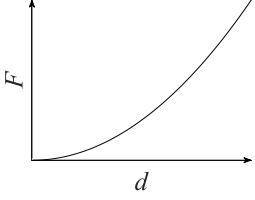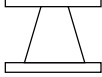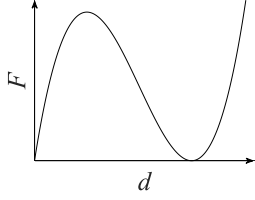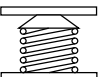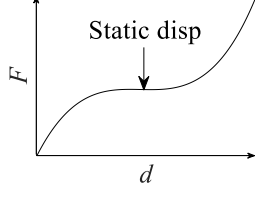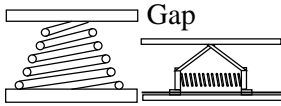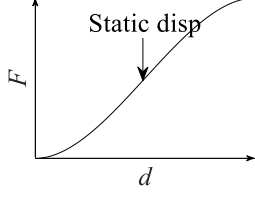
Spring	Schematic View	Force-displacement relation
V-link		
Conical		
Cone disk		
Cone disk + linear		
Conical + V-link		

Fig. 7. Nonlinear springs configurations with force displacement relation (positive indicates compression).

system at DBE displacement is the same as the initial stiffness, $K_D = K_1$. The DBE effective stiffness is related to the DBE effective frequency through

$$K_D = K_1 = 4\pi^2 m f_D^2 \tag{24}$$

The effective stiffness at BDBE displacement is established by equating the force of the effective linear system and the force of the bilinear system, i.e. $K_B u_B = K_1 u_D + K_2 (u_B - u_D)$, where u_B is the displacement at the BDBE level. With the definition of BDBE-level effective frequency, $K_B = 4\pi^2 m f_B^2$, and Equation (24),

15

$$K_2 = \frac{4\pi^2 m \left(f_B^2 u_B - f_D^2 u_D \right)}{u_B - u_D} \tag{25}$$

The effective damping ratio values at DBE and BDBE levels are $\xi_D = c_1/(4\pi m f_D)$ and $\xi_B = c_1/(4\pi m f_B)$, where $c_1 = 1{,}627$ N s/m because the damper in the NSLD system is the same as for the LSLD.

The design of the bilinear system begins with establishing its equivalency to the LSLD system at the BDBE displacement, $u_B = 0.073$ m.; therefore, $f_B = f_s = 1.8$ Hz, $\xi_B = \xi_s = 20\%$. Then, the parameters f_D and u_D must be determined. Since the damping coefficient c_1 is constant, the following expression applies at the DBE level

$$\xi_D f_D = \frac{c_1}{4\pi m} = \text{constant} \tag{26}$$

and because the effective characteristics at the DBE level must achieve an acceleration less than 1.03 g (Fig. 5), a geometric solution is used to find admissible parameters for the nonlinear spring design. In Fig. 8, the two dashed lines show the possible frequency and damping combinations that result in a peak equipment acceleration of 1.03 g and 0.76 g (which is the expected acceleration from the LSLD system) at the DBE level given the response spectra from Fig. 5. The solid line shows all possible effective characteristics that satisfy Equation (26). The intersection of the solid and 1.03 g lines leads to effective frequency 2.26 Hz and 15.5%. However, any point on the solid line below the intersection is an acceptable solution in the sense that it satisfies both the acceleration performance goal and damping equivalency at BDBE.

As illustrated in Fig. 8, if the frequency related to the initial stiffness is larger than 1.8 Hz, the bilinear elastic spring shows softening behavior. The intersection of the solid line and 0.76 g line leads to the LSLD system. If the frequency related to the initial stiffness is smaller than 1.8 Hz, the behavior of the spring is hardening. Two separate cases are studied, one with softening and one with hardening behavior: (1) NSLD$_S$: The frequency at the DBE level is selected to be $f_D = 2.0$ Hz, which has corresponding $\xi_D = 18\%$. For this combination of parameters, $u_D = 0.045$ m. Substituting these values into Equation (24) and (25) leads to $K_1 = 56{,}790$ N/m and $K_2 = 28{,}660$ N/m. Since the acceleration under the DBE level is greater than the LSLD, it is expected that although the system is designed for the performance goals, it will not perform as well as the LSLD. (2) NSLD$_H$: The frequency at the DBE level is selected as $f_D = 1.44$ Hz, with corresponding $\xi_D = 25\%$. For this combination, $u_D = 0.06$ m; resulting in $K_1 = 29{,}440$ N/m and $K_2 = 122{,}430$ N/m.
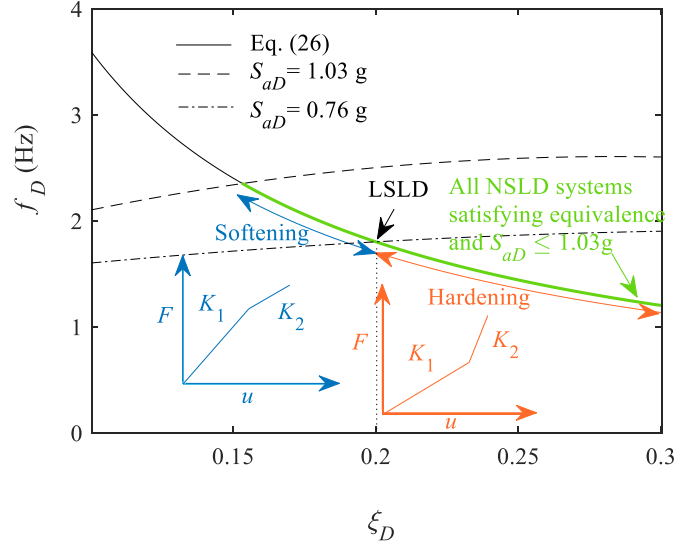
Fig. 8. Graphical design of effective system characteristics at the DBE level. Softening systems are to the left of $\xi_D = 0.2$, and hardening systems are to the right.

Table 5: The design properties of three systems

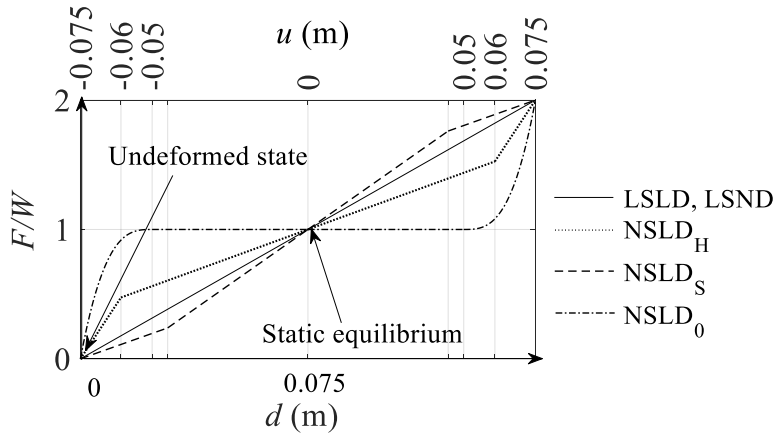|	K_1 (N/m)	K_2 (N/m)	α	c_α (N(s/m)$^\alpha$)	f_D (Hz)	f_B (Hz)	ξ_D (%)	ξ_B (%)
LSLD	46,000	-	1.0	1,627	1.8	1.8	20	20
LSND$_{0.5}$	46,000	-	0.5	1,328	1.8	1.8	25	20
LSND$_{1.5}$	46,000	-	1.5	1,957	1.8	1.8	16	20
NSLD$_S$	56,791	28,660	1.0	1,627	2	1.8	18	20
NSLD$_H$	29,440	122,430	1.0	1,627	1.44	1.8	25	20
NSLD$_0$	0	-	1.0	1,627	0	1.8	-	20

Fig. 9. Comparison of the elastic spring behavior of the vertical isolation systems (u is dynamic displacement; d is total displacement).

17

The performance of an extreme hardening system, with no initial stiffness, as proposed by Meng et al. (2015) and Zhou et al. (2019), is investigated as a separate nonlinear spring and linear damper system, identified as $NSLD_0$ (Fig. 9). The $NSLD_0$ possesses zero stiffness at DBE level and gradually shows hardening behavior to achieve the equivalency point at BDBE level. This system may be favorable for seismic isolation because it exhibits very low dynamic stiffness in static equilibrium. Table 5 summarizes the final properties of the six system designs, while Fig. 9 shows their restoring force-displacement behavior.

5. Response history analysis and results: comparison of the vertical isolation systems

To compare the performance of the vertical isolation systems, nonlinear time history analysis is conducted using the absolute vertical floor accelerations resulting from the analysis of the horizontally isolated NPP from Section 2.2.3 as input. In this cascading dynamic analysis approach, it is assumed that the dynamic responses of the internal structure of the NPP and the vertical isolated system with the MCC equipment atop it are decoupled, as the mass of the MCC is only 360 kg, while the mass of the internal structure is 50,000 tons. For the purpose of evaluating the performance of the isolation system, it is assumed that the equipment is entirely rigid. This assumption is valid provided that the nominal frequency of the isolation system is well separated from the natural frequency of the equipment. It is noted that even the frequency associated with the first stiffness of the $NSLD_H$ is low and thus is not a cause of concern for resonance in the equipment.

The equation of motion of the isolator–rigid equipment system is

$$m\ddot{u} + c_\alpha \, |\dot{u}|^\alpha \, \text{sign} \, (\dot{u}) + F = -m\ddot{u}_{fv} \tag{27}$$

where F is the restoring force of the linear or nonlinear elastic spring of the system considered (see Fig. 9), u is the displacement of the rigid equipment relative to the floor, and $\ddot{u}_{fv}$ is the absolute vertical floor acceleration at the location where the isolator–rigid equipment system is placed (see Fig. 1). It is noted that Equation (27) does not include a term corresponding to the friction force that would develop in a supplemental vertical guiding system. This force would take the form $\mu m \ddot{u}_{fh} \, \text{sign}(\dot{u})$, where μ is friction coefficient of the PTFE–stainless-steel sliding interface and $\ddot{u}_{fh}$ is the absolute horizontal floor acceleration. Considering that the friction coefficient would be in the order of 0.05, or less, that the peak of $\ddot{u}_{fh}$ is 0.32g (DBE level), and that $\ddot{u}_{fh}$ oscillates at the predominant frequency of the horizontal isolation system (2.5 s) while the vertical isolation system period is 1/1.8 Hz = 0.55 s, suggests that the contribution of this force would be negligible in the response of the system.

Equation (27) is solved, and the resulting absolute acceleration history, i.e. $\ddot{u} + \ddot{u}_{fv}$, which is the same throughout the MCC cabinet because the cabinet is assumed to be rigid, is used as input to generate 5%-damped absolute acceleration response spectra under the DBE and BDBE levels. These spectra, shown in Fig. 10 (left), provide vertical *in-cabinet* absolute accelerations which can be used to quantify demands on light components that are mounted on the MCC cabinet (e.g. contactors, relays). This cascading type of analysis assumes that the dynamic responses of the light component and the system consisting of the isolation and the MCC are decoupled, an assumption which is generally assumed to be valid when the mass ratio of the former to the latter is less than

10%. Fig. 10 (right) show the corresponding maximum displacements of the vertical isolation systems. This figure shows the boxplot of the maximum displacement including the minimum, 25th percentile, median, 75th percentile and maximum of the displacement of 30 ground motions in compression. Table 6 summarizes the results of the nonlinear time history analyses of the six systems.
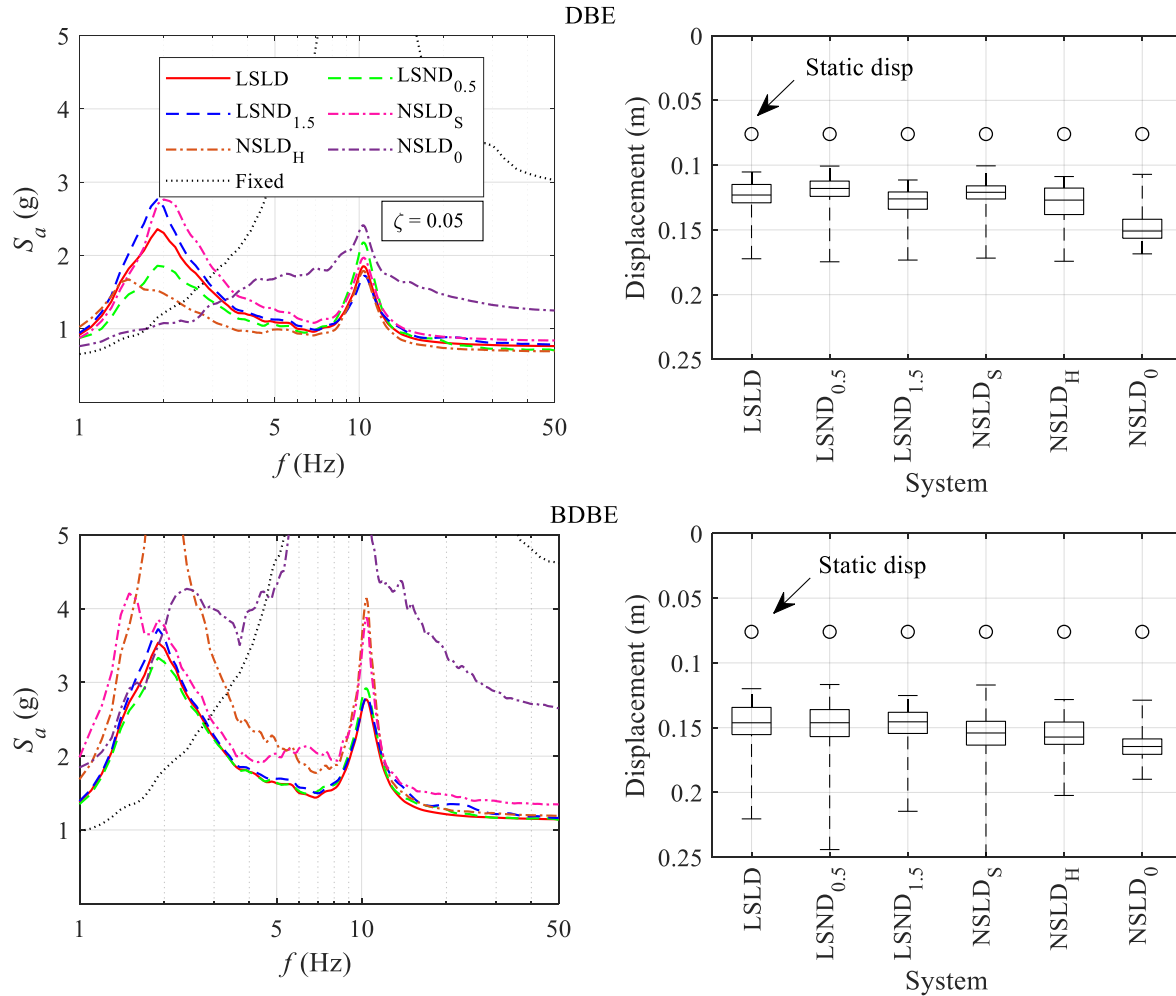

Fig. 10. Vertical in-cabinet acceleration response spectra and maximum total displacement of the isolation systems at the DBE level (top) and BDBE level (bottom). For the displacements, box plots show the median, 25th and 75th percentiles, and extreme values from the 30 analyses for each system.

The floor spectra exhibit two peaks: one near 1.8 Hz at the BDBE level, which is the BDBE vertical equipment isolation period (since equivalency between the different systems was established at the BDBE displacement), and one at near 10.4 Hz, which is the vertical frequency of the base isolated NPP. The 1–50 Hz frequency range in Fig. 10 encompasses the 5–33 Hz range where according to Huang et al., (2007) most acceleration-sensitive components in a NPP reside. All systems are effective in significantly reducing the peak equipment acceleration compared to the fixed-base case (i.e., the equipment attached directly to the floor). All systems except the $NSLD_0$ system meet the acceleration performance goal at the DBE level, and all isolation systems are

within allowable displacement limits. However, only the LSLD and $LSND_{0.5}$ systems also achieve the acceleration performance target at the BDBE level.

The LSLD system achieves peak equipment accelerations of 0.76 g and 1.14 g under the DBE and BDBE earthquakes, respectively, with median peak relative displacements of 0.123 m and 0.146 m. The $LSND_{0.5}$ system with nonlinear damping with value of $\alpha = 0.5$, exhibits marginally smaller peak equipment accelerations than the LSLD system at the DBE level. However, the $LSND_{1.5}$ with system $\alpha = 1.5$ meets the acceleration goal at the DBE level but slightly exceeds it at the BDBE level.

The $NSLD_S$ results in larger accelerations than the LSLD system with similar displacements, and while the $NSLD_H$ results in the lowest peak equipment acceleration under the DBE because of the low initial frequency, the stiffening behavior under larger displacement causes increased peak equipment accelerations at the BDBE level. The $NSLD_0$ system exceeds the acceleration performance goals at both hazard levels. The very low initial stiffness of the $NSLD_0$ leads to large displacements, which drives the system into the high tangent stiffness region under both DBE and BDBE levels, resulting in increased accelerations.

Table 6 also lists as an additional demand parameter the average spectral acceleration over the 5-33 Hz frequency range (with increment of 1 Hz) at both hazard levels. Only the $NSLD_H$ system results in reduced average acceleration relative to the LSLD under the DBE level; however, the $NSLD_H$ acceleration is considerably higher under the BDBE level. While the nonlinear damping ($LSND_{0.5}$ and $LSND_{1.5}$) give average accelerations close to the LSLD, the LSLD provides the best overall performance. In contrast, the $NSLD_0$ system results in the largest average accelerations due the significant hardening.

Table 6: Peak equipment acceleration and the displacement resulting from the six systems. (Bold numbers exceed the performance goal)

	Peak equipment acceleration (g)		Peak isolation displacement (m)		Average spectral acceleration over 5-33 Hz	
	DBE (g)	BDBE (g)	DBE (m)	BDBE (m)	DBE (g)	BDBE (g)
LSLD	0.76	1.14	0.123	0.146	0.93	1.41
$LSND_{0.5}$	0.71	1.13	0.118	0.146	0.95	1.42
$LSND_{1.5}$	0.78	**1.18**	0.126	0.145	0.97	1.49
$NSLD_S$	0.84	**1.19**	0.121	0.154	1.02	1.58
$NSLD_H$	0.69	**1.34**	0.127	0.157	0.86	1.71
$NSLD_0$	**1.25**	**2.65**	0.151	0.164	1.57	3.79

6. Discussion: Adaptive behavior in horizontal and vertical direction

While adaptive systems have been embraced for horizontal isolation, the results in the previous section have shown that adaptive system may be less beneficial than systems with linear restoring force for vertical equipment isolation. Fig. 11 shows the horizontal ground and vertical floor acceleration (left) and displacement spectra (right). For horizontal systems, adaptive isolation typically has a large initial stiffness to restrict the displacement under wind loading. Vertical isolation may also require this if it is used at the base of the structure where rocking might be a concern. Or it may be a concern in floor isolation systems where mass changes and there may be small vertical excitation from walking. However, for equipment isolation there is no specific justification to provide this large initial vertical stiffness.

Under moderate shaking, effective frequencies for horizontal isolation are typically chosen in the range of 0.25 Hz to 0.5 Hz in order to reduce accelerations. However, this can result in large displacement demands, and under very large ground motions, excessive displacements rather than accelerations become a concern. Consequently, adaptive horizontal isolation systems with hardening may be beneficial to reduce the displacements in large events. In contrast, because of the high frequency content of the vertical floor motions (Fig. 11 (Left)), the frequency of vertical isolation systems can be significantly larger (on the order of 2 Hz). Yet, in general, the displacement demand in the vertical direction is much less than in the horizontal direction (Fig. 11 (right)). While adaptive systems are beneficial for horizontal base-isolation, a simple vertical equipment isolation system consisting of a linear spring and viscous damper (linear or nonlinear) can achieve the desired performance objectives.
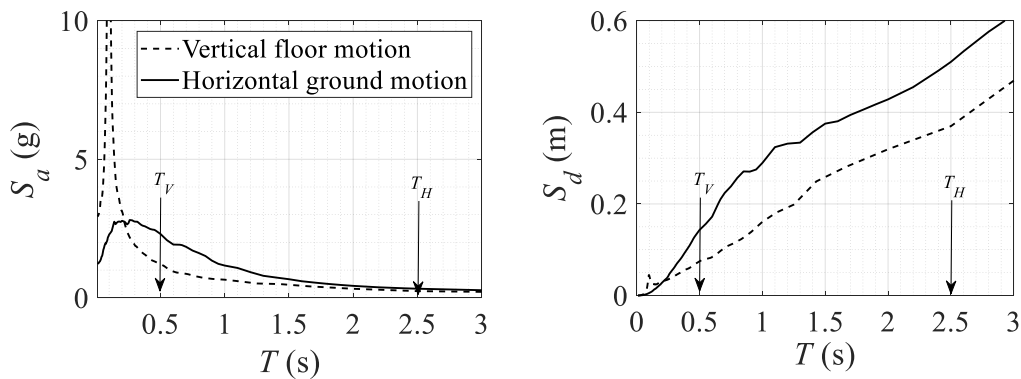

Fig. 11. Spectra for horizontal ground motions and vertical floor motions at the location of the MCC. T_H and T_V are examples of effective horizontal and vertical periods for respective isolation systems.

7. Conclusions

This paper investigated the potential benefits of adaptive vertical isolation for light equipment in a horizontally base-isolated NPP located in California. Two hazard levels were considered: the DBE with return period 10,000 years and the BDBE defined as 1.5×DBE. A motor control center (MCC), categorized as very important electrical equipment with low seismic capacity, was selected to be vertically isolated. The experimental fragility curve was used to define the

engineering demand parameter corresponding to the performance objectives under DBE and BDBE levels for the MCC. Nonlinear dynamic analyses were conducted to compute the floor motions at the location of the MCC. Six isolation systems were considered: linear spring and linear damper (LSLD), linear spring and nonlinear damper with $\alpha = 0.5$ (LSND$_{0.5}$), linear spring and nonlinear damper with $\alpha = 1.5$, nonlinear spring and linear damper with softening behavior (NSLD$_S$), nonlinear spring and linear damper with hardening behavior (NSLD$_H$), and nonlinear spring and linear damper with zero stiffness (NSLD$_0$). The important observations of this study are summarized as follows:

(1) Equipment at higher levels of the internal structure of NPP experience large vertical accelerations regardless of the design of LRB due to the high frequency content of vertical component of ground motions. This large amplification shows a potential need for the usage of vertical equipment isolation system.

(2) All equipment isolation systems except NSLD$_0$ system met the acceleration goal at the DBE level. The NSLD$_H$ showed the lowest peak equipment acceleration at DBE level. However, this system did not achieve the acceleration goal at BDBE level. The LSLD and LSND$_{0.5}$ were the only systems that met the acceleration goals under both hazard levels.

(3) All of the equipment isolation systems operated within their allowable displacement limits for the BDBE level. The stiffening regime of the adaptive systems was not necessary because the vertical displacement demands are moderate compared to horizontal displacement demands. Hence, a spring and a damper (linear or nonlinear) can accommodate the displacement demand.

(4) The average spectral acceleration over 5-33 Hz was studied to evaluate the isolation systems to capture the applicability of the system to a wider range of equipment. The results showed that the nonlinear damper had a minor benefit on this demand (less than 2%). The nonlinear spring increased this demand significantly.

References

American Society of Civil Engineers (ASCE), 2005. Seismic Design Criteria for Structures, Systems, and Components in Nuclear Facilities (ASCE/SEI 43-05). Reston, VA, USA.

American Society of Civil Engineers (ASCE), 2016. Minimum Design Loads and Associated Criteria for Buildings and other Structures (ASCE/SEI 7-16). Reston, VA, USA.

Asai, T., Araki, Y., Masui, T., Yoshida, N., 2008. Vertical vibration isolation device using constant load supporting mechanism. Journal of Structural and Constructional Engineering. 73(631), 1511-1518.

Asher, J. W., Young, R. P., Ewing, R. D., 1996. Seismic isolation design of the San Bernardino county medical center replacement project. The Structural Design of Tall Buildings. 5(4), 265-279.

Bandyopadhyay, K., Hofmayer, C., 1986. Seismic fragility of nuclear power plant components. Phase I. NUREG/CR-465g, BNL-NUREG-52007, Vol.2. USA.

Becker, L. E., Cleghorn, W., 1992. On the buckling of helical compression springs. International Journal of Mechanical Sciences. 34(4), 275-282.

Becker, T. C., Bao, Y., Mahin, S. A., 2017. Extreme behavior in a triple friction pendulum isolated frame. Earthquake Engineering and Structural Dynamics. 46(15), 2683-2698.

Christopoulos, C., Filiatrault, A., 2008. Principles of Passive Supplemental Damping and Seismic Isolation. IUSS Press, Italy.

Cimellaro, G. P., Domaneschi, M., Warn, G., 2019. Three-dimensional base isolation using vertical negative stiffness devices. Journal of Earthquake Engineering. In-press.

Constantinou, M. C., Kartoum, A., Kelly, J. M., 1992. Analysis of compression of hollow circular elastomeric bearings. Engineering Structures. 14(2), 103-111.

Fenz, D. M., Constantinou, MC. 2007. Spherical sliding isolation bearings with adaptive behavior: Theory. Earthquake Engineering and Structural Dynamics. **37**(2):163–183.

Furukawa, S., Sato, E., Shi, Y., Becker, T., Nakashima, M., 2013. Full-scale shaking table test of a base-isolated medical facility subjected to vertical motions. Earthquake Engineering and Structural Dynamics. 42(13), 1931-1949.

Gent, A., 1990. Cavitation in rubber: a cautionary tale. Rubber Chemistry and Technology. 63(3), 49-53.

Guzman Pujols, J. C., Ryan, K. L., 2018. Computational simulation of slab vibration and horizontal-vertical coupling in a full-scale test bed subjected to 3D shaking at E-Defense. Earthquake Engineering and Structural Dynamics. 47(2), 438-459.

Huang, Y.-N., Whittaker, A. S., Luco, N., 2008. Performance assessment of conventional and base-isolated nuclear power plants for earthquake and blast loadings. MCEER-08-0019. University at Buffalo, USA.

Huang, Y.-N., Whittaker, A. S., Luco, N., 2011. A probabilistic seismic risk assessment procedure for nuclear power plants:(II) Application. Nuclear Engineering and Design. 241(9), 3985-3995.

Huang, Y. N., Whittaker, A. S., Constantinou, M. C., Malushte, S., 2007. Seismic demands on secondary systems in base-isolated nuclear power plants. Earthquake Engineering and Structural Dynamics. 36(12), 1741-1761.

Huang, Y. N., Whittaker, A. S., Kennedy, R. P., Mayes, R. L., 2013. Response of base-isolated nuclear structures for design and beyond-design basis earthquake shaking. Earthquake Engineering and Structural Dynamics. 42(3), 339-356.

Japan Nuclear Energy Safety Organization (JNSE), 2013. Proposal of Technical Review Guidelines for Structures with Seismic Isolation (JNES-RC-2013-1002). Japan.

Kelly, J. M., Konstantinidis, D., 2011. Mechanics of Rubber Bearings for Seismic and Vibration Isolation. John Wiley & Sons, USA.

Kumar, M., Whittaker, A. S., Constantinou, M. C., 2015a. Seismic isolation of nuclear power plants using sliding bearings. MCEER-15-0006. University at Buffalo, USA.

Kumar, M., Whittaker, A. S., Constantinou, M. C., 2015b. Seismic isolation of nuclear power plants using elastomeric bearings. MCEER-15-0008. University at Buffalo, USA.

Kumar, M., Whittaker, A. S., Constantinou, M. C., 2017. Extreme earthquake response of nuclear power plants isolated using sliding bearings. Nuclear Engineering and Design. 316, 9-25.

Lee, D., Constantinou, M. C., 2017. Development and validation of a combined horizontal-vertical seismic isolation system for high-voltage power transformers. MCEER-17-0007. University at Buffalo, USA.

Lee, D., Constantinou, M. C., 2018. Combined horizontal–vertical seismic isolation system for high-voltage–power transformers: development, testing and validation. Bulletin of Earthquake Engineering. 16(9) 4273–4296.

Lin, W. H., Chopra, A. K., 2002. Earthquake response of elastic SDF systems with non-linear fluid viscous dampers. Earthquake Engineering and Structural Dynamics. 31(9), 1623-1642.

McVitty, W. J., Constantinou, M. C, 2015. Property modification factors for seismic isolators: design guidance for buildings. MCEER-15-0005. University at Buffalo, USA.

Medel-Vera, C., Ji, T., 2015. Seismic protection technology for nuclear power plants: a systematic review. Journal of Nuclear Science and Technology. 52(5), 607-632.

Meng, L., Sun, J., Wu, W., 2015. Theoretical design and characteristics analysis of a quasi-zero stiffness isolator using a disk spring as negative stiffness element. Shock and Vibration. ID: 813763.

Morgan, T. A., Mahin, S. A., 2010. Achieving reliable seismic performance enhancement using multi-stage friction pendulum isolators. Earthquake Engineering and Structural Dynamics. 39(13), 1443-1461.

Mori, S., Suhara, I., Saruta, M., Okada, K., Tomizawa, T., Tsuyuki, Y., Fujita, T. 2012. Simulation analysis of free vibration test in a building Chisuikan using three-dimensional seismic base isolation system. Proc. 15th World Conference on Earthquake Engineering, Lisbon, Portugal.

Morishita, M.,Inoue, K., Fujita, T., (2004). Development of three-dimensional seismic isolation systems for fast reactor applications. Journal of Japan Association for Earthquake Engineering. 4(3), 305-310.

Najafijozani, M., 2019. Adaptive Vertical Seismic Isolation for Equipment (Thesis). McMaster University. Canada.

Nawrotzki, P., Siepe, D. 2014. Structural challenges of power plants in high seismic areas. Proc. Second European Conference on Earthquake Engineering and Seismology, Istanbul, Turkey.

Open System for Earthquake Engineering Simulation (Computer software), 2018.

Papazoglou, A., Elnashai, A., 1996. Analytical and field evidence of the damaging effect of vertical earthquake ground motion. Earthquake Engineering and Structural Dynamics. 25(10), 1109-1137.

Radford, T., 2015. Electrical Cabinet Seismic Frequency Estimation. EPRI Webinar, USA.

Reed, J. W., Kennedy, R. P., 1994. Methodology for developing seismic fragilities. TR-103959. EPRI, California, USA.

Rodriguez, E., Paredes, M., Sartor, M., 2006. Analytical behavior law for a constant pitch conical compression spring. Journal of Mechanical Design. 128(6), 1352-1356.

Saudy, A., 2017. Personal Communication. Kinectrics Inc.

Shigley, J. E., 2011. Shigley's Mechanical Engineering Design. McGraw-Hill Education, USA.

Soong, T., Constantinou, M. C., 1994. Passive and Active Structural Vibration Control in Civil Engineering. Springer, USA.

Suhara, J., Tamura, T., Ohta, K., Okada, Y., Moro, S. 2003. Research on 3-D base isolation system applied to newpower reactor 3-D seismic isolation device with rolling seal type air spring: part 1. 17th Structural Mechanics in Reactor Technology (SMiRT 17), paper # K09-4, Prague, Czech Republic.

Tsujiuchi, N., Ito, A., Sekiya, Y., Nan, C., Yasuda, M., 2016. Characterization and performance evaluation of a vertical seismic isolator using link and crank mechanism. Journal of Physics: Conference Series. 744(1), 012232.

Tsutsumi H, Yamada H, Mori K, Ebisawa K, Shibata K. 2000. Characteristics and dynamic response of 3-Dcomponent base isolation system using ball bearings and air springs. JAERI-Tech 2000-086 in Japa-nese, Japan Atomic Energy Research Institute, Japan.

Ueda, M., Ohmata, K., Yamagishi, R., Yokoo, J., 2007. Vertical and three-dimensional seismic isolation tables with bilinear spring force characteristics: for which a Λ-shaped link mechanism is used. Trans. Japan Society of Mechanical Engineers, Series C. 73(735), 2932-2939.

Van Engelen, N. C., Konstantinidis, D., Tait, M. J., 2016. Structural and nonstructural performance of a seismically isolated building using stable unbonded fiber-reinforced elastomeric isolators. Earthquake Engineering and Structural Dynamics. 45(3), 421-439.

Wakabayashi, N., Ohmata, K., Masuda, T., 2009. Vertical seismic isolation system using V-shaped link mechanism. Journal of Japan Society of Mechanical Engineers. 75, 26-32.

Wu, M., Hsu, W., 1998. Modelling the static and dynamic behavior of a conical spring by considering the coil close and damping effects. Journal of Sound and Vibration. 214(1), 17-28.

Yang, T. Y., Konstantinidis, D., Kelly, J. M., 2010. The influence of isolator hysteresis on equipment performance in seismic isolated buildings. Earthquake Spectra. 26(1), 275-293.

Zhou, Y., Chen, P., Mosqueda, G., 2019. Analytical and numerical investigation of Quasi-Zero Stiffness Vertical Isolation System. Journal of Engineering Mechanics. 145(6), 04019035.

Zhou, Z., Wong, J., Mahin, S., 2016. Potentiality of using vertical and three-dimensional isolation systems in nuclear structures. Nuclear Engineering and Technology. 48(5), 1237-1251.